PAPER

Accurate and Robust Automatic Target Recognition Method for SAR Imagery with SOM-Based Classification

Shouhei KIDERA[†a)] ***and*** **Tetsuo KIRIMOTO**[†]**,** ***Members***

SUMMARY Microwave imaging techniques, in particular synthetic aperture radar (SAR), are able to obtain useful images even in adverse weather or darkness, which makes them suitable for target position or feature estimation. However, typical SAR imagery is not informative for the operator, because it is synthesized using complex radio signals with greater than 1.0 m wavelength. To deal with the target identification issue for imaging radar, various automatic target recognition (ATR) techniques have been developed. One of the most promising ATR approaches is based on neural network classification. However, in the case of SAR images heavily contaminated by random or speckle noises, the classification accuracy is severely degraded because it only compares the outputs of neurons in the final layer. To overcome this problem, this paper proposes a self organized map (SOM) based ATR method, where the binary SAR image is classified using the unified distance matrix (U-matrix) metric given by the SOM. Our numerical analyses and experiments on 5 types of civilian airplanes, demonstrate that the proposed method remarkably enhances the classification accuracy, particular in lower S/N situations, and holds a significant robustness to the angular variations of the observation.

key words: *automatic target recognition, neural network, self organizing map (SOM), synthetic aperture radar (SAR), SAR imagery, U-matrix metric*

1. Introduction

Satellite-borne or ground-based microwave radar systems are essential tools for long range assessments, even in an optically harsh environment, such as adverse weather, darkness or strong backlight situations. This property is indispensable for emerging target identification requirements, in disaster area assessment, coast guard security, or air-traffic control, where the targets such as buildings, ships or airplanes need to be correctly identified and located. For such applications, there has been major progress in SAR-based [1] imaging techniques and its spatial resolution has been improved because of recent advances in measurement devices [2], [3]. However, it is still difficult for an operator to recognize targets in high-resolution SAR images, compared to optically acquired images, because the SAR image is generated by complex signals of greater than 1 m wavelength.

To address this issue, various automatic target recognition (ATR) schemes for SAR imagery have been proposed. Most are based on a machine learning approach such as a neural network [4], [5] or support vector machine (SVM) [6]. In particular, neural network based approaches have improved considerably, e.g. employing a range profile [7], or exploiting polarimetric data [8], [9]. While these approaches have provided significant results for typical ATR systems, in the case of degraded SAR images contaminated by random or speckle noises, this approach fails to work well, because its classification mainly relies on the assessment only for the difference of outputs obtained from test and training inputs.

This paper applies a self-organized map (SOM), based on topological clustering, as a solution to the ATR problem [10], [11]. To deal with the ATR issue, this method incorporates a classification process into SOM known as a supervised SOM [12], [13]. One application based on the SOM classification has been reported for urban area measurement using polarimetric radar, where an open-space, artificial structure or vegetation is appropriately classified by employing Stokes vectors [14], [15]. Note that this method adds the output layer (the Grossberg layer) from the Kohonen layer (SOM) to classify the Stokes vector, which is regarded as an extended type of the existing neural network approaches. It does not then proactively use the topological feature of SOM. To extract the maximum potential from SOM classification, this paper exploits the topological characteristic of SOM by introducing the criteria of the U-matrix metric calculated on the SOM [16], [17]. In detail, the SOM is initially generated by training SAR images with the batch-learning SOM (BLSOM) algorithm [18], where the clustering result can be impervious to the order of the training sequence. This method then classifies the SAR images into an appropriate category, introducing the path integration along the U-matrix potential field, the barrier of which effectively separates each training image. A distinct advantage of this method is that it accurately classifies the noisy SAR images degraded by random or speckle noises, because it evaluates not only the Euclidean distance between the node locations, but also considers the topological distribution of the U-matrix potential field. Finally, numerical analyses of the experimental data obtained from 1/200 scaled-down models, investigating the 5 civilian aircraft(B-747, B-777, B-787, DC-10 and A320), demonstrate that the proposed ATR method successfully classifies SAR imagery, even in quite noisy environment, and holds a certain amount of robustness to the angle variations of aircraft nose.

2. Observation Model and SAR Image Binarization

Figure 1 shows the observation geometry. It assumes a mono-static radar, where a set of transmitting and receiving antenna is scanned along the straight line as $y = y_0$, $z = z_0$,

Manuscript received March 30, 2012.
Manuscript revised June 28, 2012.

[†]The authors are with the Graduate School of Informatics and Engineering, The University of Electro-Communications, Chofu-shi, 182-8585 Japan.
a) E-mail: kidera@ee.uec.ac.jp

DOI: 10.1587/transcom.E95.B.3563

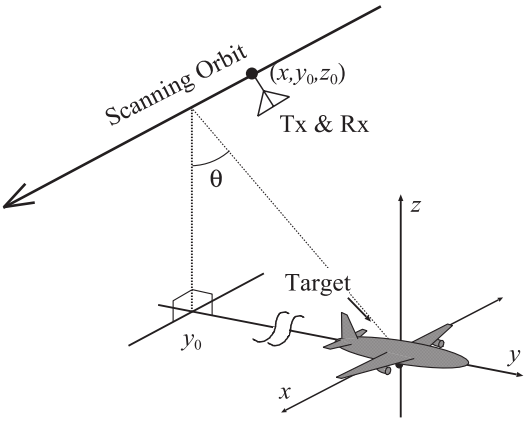

Fig. 1 System and geometry model.

and the location of antenna is set at (x, y_0, z_0). A target with arbitrary shape is located in the vicinity of the origin. The propagation speed of the microwave is a known constant. The off-nadir angle is denoted by θ. Each antenna receives the complex-valued reflection signals $s(x, f)$ at each frequency f, which are swept in the finite frequency range with the pulse compression technique. The SAR complex image focused on the $z = 0$ plane is defined as $I(x, y)$. For SAR image generation, the back projection method [19] is adopted, because this method maintains the spatial resolution and accuracy even for various observation geometries, compared with the other chirp-scaling or a range Doppler based schemes. To deal with target recognition, the SAR image is binarized as:

$$I^{\mathrm{bi}}(x, y) = \begin{cases} 1 & (|I(x, y)| \geq I_{\mathrm{th}}), \\ 0 & (\text{Otherwise}), \end{cases} \tag{1}$$

where the binarization threshold I_{th} is determined by Otsu's discriminant analysis method [20]. This method automatically determines the above threshold I_{th} by maximizing the separation metrics as the ratio of a between-class variance and a within-class variance.

3. Conventional Method

As one of the most typical approaches to resolve the ATR issues, the neural network based method using back propagation training is introduced in this section [21]. For simplicity, the three layers model, i.e. input, hidden and output layers, is employed. Figure 2 shows the topology of this neural network model. The binarized SAR image $I^{\mathrm{bi}}(x, y)$ is rearranged as a single row matrix, $\boldsymbol{x} = [x_1, \cdots, x_{N_1}] \in \mathbb{R}^{1\times N_1}$, where N_1 denotes the total number of SAR image pixels. The kth training data is also defined as $\boldsymbol{x}_k^{\mathrm{tr}} = \left[x_{k,1}^{\mathrm{tr}}, \cdots, x_{k,N_1}^{\mathrm{tr}}\right], \in \mathbb{R}^{1\times N_1}$ $(k = 1, \cdots, N_{\mathrm{tr}})$, where N_{tr} is the total number of the training data. The output of the mth layer is defined as $\boldsymbol{u}(m) = [u_1(m), \cdots, u_{N_m}(m)] \in \mathbb{R}^{1\times N_m}$, where N_m denotes the total number of neurons at the mth layer. The output of the jth neuron in mth layer is defined as $u_j(m)$,

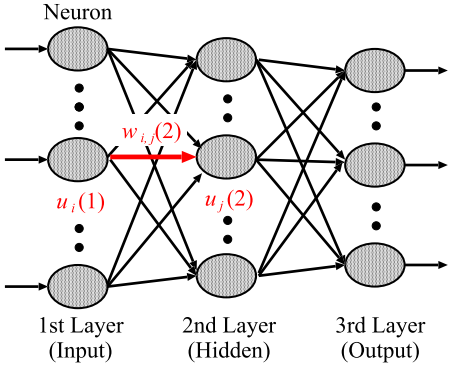

Fig. 2 Topology of neural network in three layers model.

$$u_j(m) = x_j, \quad (m = 1) \tag{2}$$

$$u_j(m) = \frac{1}{1+\exp\left(-\sum_{i=1}^{N_{m-1}} w_{i,j}(m)u_i(m-1)\right)}, \quad (m = 2, 3) \tag{3}$$

where $w_{i,j}(m)$ denotes the weight coefficient from $u_i(m-1)$ to $u_j(m)$ as shown in Fig. 2.

In the training process, the back propagation algorithm [21] is adopted, which is based on minimization the following quantity E,

$$E = \sum_{k=1}^{N_{\mathrm{tr}}} \left\|\boldsymbol{u}_k^{\mathrm{tr}}(3) - \boldsymbol{u}(3)\right\|^2, \tag{4}$$

where $\boldsymbol{u}_k^{\mathrm{tr}}(3)$ denotes the output values of the final layer, when $\boldsymbol{x}_k^{\mathrm{tr}}$ is input. The optimal update amount for the weight $w_{i,j}(m)$ is determined by the gradient approach to attain the minimum value of E,

$$\Delta w_{i,j}(m; t+1) = \eta \sum_{k=1}^{N_{\mathrm{tr}}} \zeta_{k,j}(m)u_i(m-1) + \alpha \Delta w_{i,j}(m; t), \tag{5}$$

where $\Delta w_{i,j}(m; t)$ denotes the update amount of the weight $w_{i,j}(m)$ in the tth training trial, η is the constant training coefficient and α means memory coefficient for the previous weight. Here, $\zeta_{k,j}(m)$ is defined as

$$\zeta_{k,j}(m) = \begin{cases} z_j(m) \sum_{l=1}^{N_{m+1}} \zeta_{k,l}\,(m+1) w_{j,l}\,(m+1; t), & (m=2) \\ z_j(m)\left(u_{k,j}^{\mathrm{tr}}\,(m) - u_j(m)\right), & (m=3) \end{cases} \tag{6}$$

where $z_j(m) = u_j(m)(1-u_j(m))$ is defined. The above update is recursively carried out with the T_{NN} times.

Next, this method classifies the unknown image data $\boldsymbol{x}$ into the $K_{\mathrm{opt}}^{\mathrm{NN}}$th group of the training data as,

$$K_{\mathrm{opt}}^{\mathrm{NN}} = \arg\min_{1\leq k\leq N_{\mathrm{tr}}} \frac{\|\boldsymbol{u}(3) - \boldsymbol{u}_k^{\mathrm{tr}}(3)\|}{\|\boldsymbol{u}_k^{\mathrm{tr}}(3)\|}, \tag{7}$$

where $\boldsymbol{u}_k(3)$ denotes the output values of the final layer,

when $\boldsymbol{x}$ is input to the neural network after the training process. While some literature based on this approach verified that they could effectively discriminate unknown images in typical situations [4], [5], in the case of noisy SAR images contaminated by random or speckle noises, this method hardly obtains a sufficient accuracy for target classification even with the optimzized parameters such as η or α, because it mainly adopt the classification comparing the output differences between the test and training at the final layer.

4. Proposed Method

As a solution to the aforementioned difficulties, this paper proposes the SOM based classification method. Note that, while the SOM itself does not require the training data, it can cluster the input data in a lower-dimensional map (for example a 2-dimensional map). In recent years, several literature using SOM with training data called supervised-SOM have been reported in pattern recognition issues [12], [13]. To address the ATR for SAR imagery, this paper adopts a similar approach in the above literature. That is, in the first stage, the SOM is generated using the training SAR imagery $\boldsymbol{x}_k^{\mathrm{tr}}$ as defined in Sect. 3. The unknown input data are then classified into a specific category, considering the topological distribution of the U-matrix potential field given by the SOM.

4.1 Training Process

First, the training process in the proposed method is described as follows. The training binarized SAR images are set as $\boldsymbol{x}_k^{\mathrm{tr}}, (k = 1, \cdots, N_{\mathrm{tr}})$. The SOM consists of $M_{\mathrm{X}} \times M_{\mathrm{Y}}$ nodes (neurons) located in the 2-dimensional rectangular grid with the coordinates (x, y), where M_{X} and M_{Y} denote the numbers of nodes along x and y axes. The location of each node is defined as $\boldsymbol{p}$, and the node has the output vector defined as $\boldsymbol{y}(\boldsymbol{p}; t) \in \mathbb{R}^{1 \times N_{\mathrm{I}}}$, where t denotes the number of the training trial. For effective separation for node locations of each training image, an initial output for each node is defined using a linear mixture of the training images as,

$$\boldsymbol{y}(\boldsymbol{p}; 0) = \frac{\sum_{k=1}^{N_{\mathrm{tr}}} a_k(\boldsymbol{p}) \boldsymbol{x}_k^{\mathrm{tr}}}{\sum_{k=1}^{N_{\mathrm{tr}}} a_k(\boldsymbol{p})}, \tag{8}$$

where $a_k(\boldsymbol{p})$ has a uniform distribution for [0, 1] with a variant of node locations.

The actual procedure is summarized as follows.

Step 1). Initial images for all nodes are determined in Eq. (8).

Step 2). For the kth training data $\boldsymbol{x}_k^{\mathrm{tr}}$, the location of the winner node denote as $\hat{\boldsymbol{p}}_k(t)$ is determined by:

$$\hat{\boldsymbol{p}}_k(t) = \arg\min_{\boldsymbol{p} \in \Omega} \| \boldsymbol{y}(\boldsymbol{p}; t) - \boldsymbol{x}_k^{\mathrm{tr}} \|, \tag{9}$$

where Ω express the region of SOM, and $\| * \|$ denotes the Euclidean norm.

Step 3). After calculating $\hat{\boldsymbol{p}}_k(t)$ for all the training data, the output of each node is updated by:

$$\boldsymbol{y}(\boldsymbol{p}; t+1) = \boldsymbol{y}(\boldsymbol{p}; t) + \frac{\sum_{k=1}^{N_{\mathrm{tr}}} h\left(\hat{\boldsymbol{p}}_k(t), \boldsymbol{p}\right) \left(\boldsymbol{x}_k^{\mathrm{tr}} - \boldsymbol{y}(\boldsymbol{p}; t)\right)}{\sum_{k=1}^{N_{\mathrm{tr}}} h\left(\hat{\boldsymbol{p}}_k(t), \boldsymbol{p}\right)}, \tag{10}$$

where $h\left(\hat{\boldsymbol{p}}_k(t), \boldsymbol{p}\right)$ is the neighbouring function as

$$h\left(\hat{\boldsymbol{p}}_k(t), \boldsymbol{p}\right) = \beta(t) \exp\left(-\frac{\|\hat{\boldsymbol{p}}_k(t) - \boldsymbol{p}\|^2}{2\sigma(t)^2}\right). \tag{11}$$

Here, $\sigma(t) = \sigma_0(1 - t/2T_{\mathrm{som}}), \beta(t) = \beta_0(1 - t/2T_{\mathrm{som}})$ are set, for simplicity, where T_{som} denotes the total number of training trials. $\sigma(t)$ denotes the affecting region of the neighboring function, and $\beta(t)$ presents a learning coefficient. Both $\sigma(t)$ and $\beta(t)$ should decrease monotonically with trial [11], and are empirically determined.

Step 4). Steps 2) to 3) are repeated until the trial number reaches T_{som}.

We then adopt the batch learning (BL) approach in Step 3) for creating the SOM [18], which has the distinct advantage that the final SOM is not relevant to the order of the training data, that is, the SOM is updated after all the input data are evaluated. Moreover, in calculating the Euclidean distance between the nodes in Eq. (11), it assumes a periodical structure of the SOM, to avoid the edge convergence of each winning node. Figure 3 shows the periodical structure of SOM, where the eight subsidiary SOMs (Sub SOM) are adjacently located to the actual SOM (Main SOM). As shown in Fig. 3, the actual distance between the node $\boldsymbol{p}_A$ and $\boldsymbol{p}_X$ is not measured as $\|\boldsymbol{p}_A - \boldsymbol{p}_X\|$ but as $\|\boldsymbol{p}_{A^1} - \boldsymbol{p}_X\|$ in calculating Eq. (11),

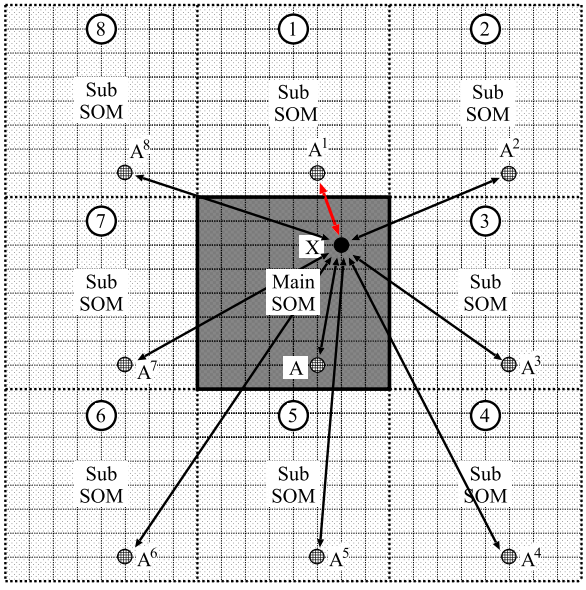

Fig. 3 Periodical structure of SOM and the actual distance between nodes of $\boldsymbol{p}_A$ and $\boldsymbol{p}_X$.

which is the minimum of $\|\boldsymbol{p}_X - \boldsymbol{p}_{A^i}\|$, $(i = 1, \cdots, 8)$.

4.2 Classification Process

The classification process is now introduced. In this method, the U-matrix potential field derived in [17], is proactively used for classification, which is normally referenced as the visualization of the data discrepancy of each node, not only Euclidean distance between them. In preparation, each winner node for the kth training data in the final SOM is determined as $\hat{\boldsymbol{p}}_k(T_{\mathrm{som}})$. For the unknown input as $\boldsymbol{x}$, the location of the winner neuron $\hat{\boldsymbol{p}}(\boldsymbol{x})$ is determined by:

$$\hat{\boldsymbol{p}}(\boldsymbol{x}) = \arg\min_{\boldsymbol{p}\in\Omega} \|\boldsymbol{y}(\boldsymbol{p}; T_{\mathrm{som}}) - \boldsymbol{x}\|. \tag{12}$$

One of the traditional metric is the Euclidean distance between $\hat{\boldsymbol{p}}(\boldsymbol{x})$ and $\hat{\boldsymbol{p}}_k(T)$. However, this metric does not consider the potential barrier generated by the U-matrix, which enables us to quantitatively assess the actual discrepancy among $\boldsymbol{y}(\boldsymbol{p}; T)$ of each node. To extract a maximum potential of the SOM feature, $\boldsymbol{x}$ is classified into the $K_{\mathrm{opt}}^{\mathrm{som}}$ th group of training data with the U-matrix metric as,

$$K_{\mathrm{opt}}^{\mathrm{som}} = \arg\min_{1\le k\le N_{\mathrm{tr}}} \left\{ \min_{C(k,\boldsymbol{x})} \int_{C(k,\boldsymbol{x})} U(\boldsymbol{p}) \mathrm{d}s \right\}, \tag{13}$$

where $C(k, \boldsymbol{x})$ denotes all possible paths from $\hat{\boldsymbol{p}}_k(T_{\mathrm{som}})$ to $\hat{\boldsymbol{p}}(\boldsymbol{x})$ on U-matrix field as $U(\boldsymbol{p})$, which is detailed in Appendix, and $\mathrm{d}s = \|\mathrm{d}\boldsymbol{p}\|$. In minimizing the value of the above integration, all possible paths are investigated from the node $\hat{\boldsymbol{p}}(\boldsymbol{x})$ to $\hat{\boldsymbol{p}}_k(T_{\mathrm{som}})$ as shown in Fig. 4, where the periodical structure of SOM as in Fig. 3 is also considered. Figure 5 summarizes the procedure of the proposed method.

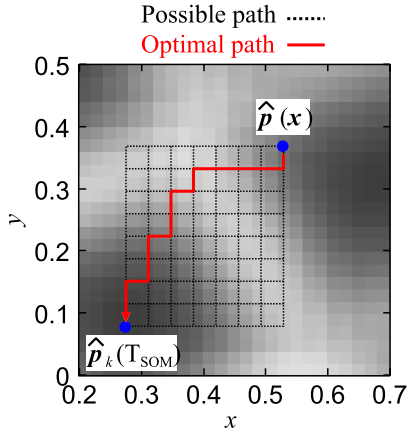

Fig. 4 Possible and optimum path in minimizing the right term of Eq. (13).

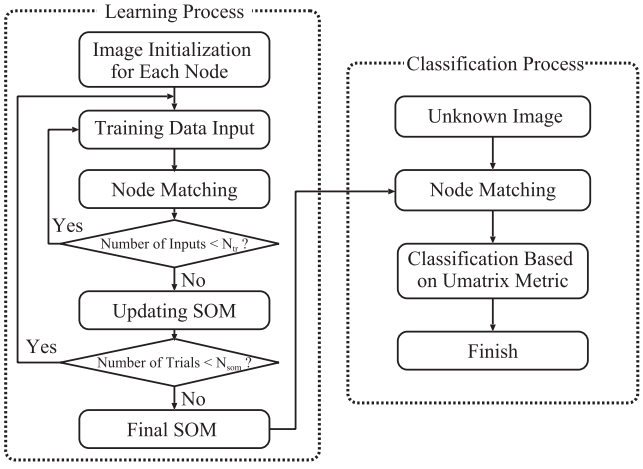

Fig. 5 Flowchart of the proposed method.

5. Performance Evaluation Using Experimental Data

This section presents the validation of each method using the experimental data. Figure 6 shows the experimental scenario. The transmitting and receiving antennas are two horn antennas with 3 dB beam widths of 27 °, and a separation of 48 mm. On the transmitter side, a 20 dB amplifier is inserted to obtain a sufficient echo from the targets. The received data each frequency are acquired by a vector network analyzer (VNA). The both transmitting and receiving polarizations are a linear in the direction of y-z plane, namely, vertical polarization. To adjust the possible experimental setup, a 1/200 downscaled model for the target, geometry and spatial resolution is adopted, because an X-band radar system is assumed in this study, where the spatial resolution is around 2 m and the center frequency is around 10 GHz. However, with respect to the center frequency of the transmitted signal, it is difficult to adjust it to a realistic value (more than THz frequency required in the 1/200 model) because of the limitations of the experimental device, and a 1/3 downscale model is used. The minimum and maximum frequencies in the VNA are 24 and 40 GHz, where the spatial resolutionΔR is 9.375 mm, and the central wavelength λ is also 9.375 mm. The center locations of the transmitting and receiving antennas are set at $(0, y_0, z_0) = (0.0\Delta R, 112.0\Delta R, 79.1\Delta R)$, and the off-nadir angle θ is 54.7 degree. The 5 different types of aircrafts are 1/200 scaled-down plastic models of the B-747, B-777, B-787, DC-10 and A320, with iron-coated surfaces. Figure 7 shows the optical images for these airplanes. To

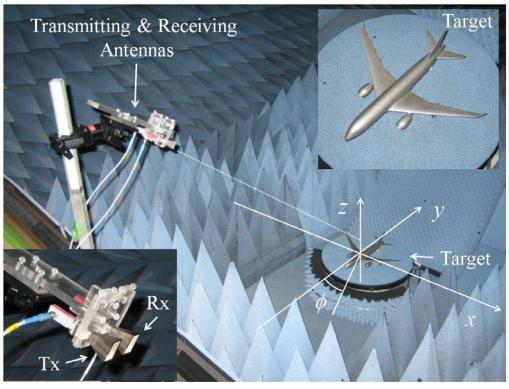

Fig. 6 Experimental scene.

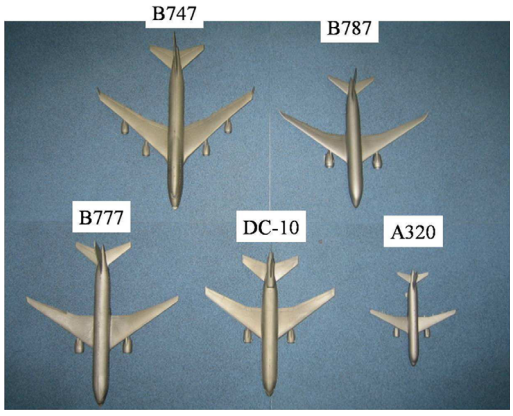

Fig. 7 Optical images for each type of airplane.

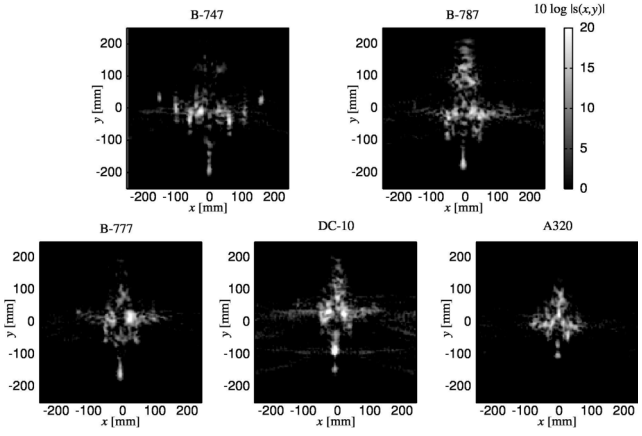

Fig. 8 SAR images for each airplane.

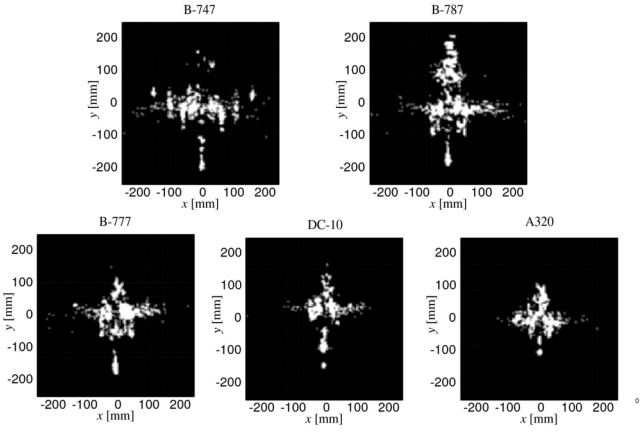

Fig. 9 Binarized images for each airplane.

enhance the signal to clutter ratio, the received signals from a scene with no target are eliminated from the observed signals when a target exists.

Figures 8 and 9 illustrate the absolute values of the complex SAR images and the binarized images for each airplane, where the angle of the airplane nose as ϕ as shown in Fig. 6, is set to 0°. As described in Sect. 2, each complex

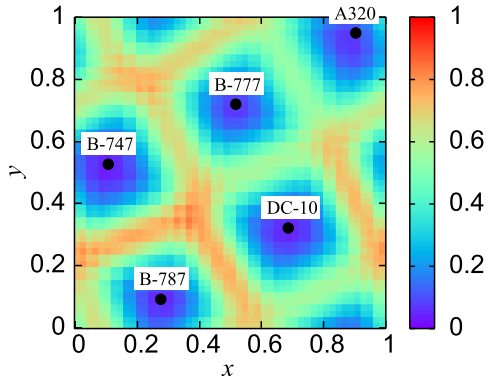

Fig. 10 U-matrix potential field created by SOM and winner nodes for each training data.

SAR image is generated by the back projection algorithm, and its binary threshold I_{th} is determined by the Otsu's discriminant analysis method. As shown in these figures, while the appearances of each SAR or binarized image are different from each other, it is naturally difficult for an operator, who is accustomed to an optical image, to identify the model of airplane. Figure 10 shows the U-matrix potential field created by the SOM and the winner node for each airplane. $N_1 = 251 \times 251 = 63001$, $M_X = M_Y = 26$, $0 \le \|\boldsymbol{p}\| \le 1$, $\sigma_0 = 0.2, \beta_0 = 0.5$ and $T_{\text{som}} = 100$ are set. As shown in this figure, the winner node of $\hat{\boldsymbol{p}}_k(T_{\text{som}})$ for each training data set is located to maintain a certain distance from other nodes, and the U-matrix potential creates a significant barrier between them.

5.1 Robustness to Noises

First, we investigate the classification performance for each method, in the case that the obtained SAR images are contaminated by numerically adding random noises. To generate the contaminated input images, white Gaussian complex components are directly added to each complex SAR image. Here, S/N is defined as the ratio of the average power of the target region to that of the non-target region in the image domain. This paper assumes that target detection has been completed, and an orientation for each target can be estimated within a certain level of error as 30°. We then only discuss the classification accuracy of the airplane types, and do not deal with a target identification for each type of airplane. Figure 11 shows the correct classification probability for airplane type (abbreviated as P_{CC}) versus the S/N for each aircraft target model, obtained using the neural network based conventional method and our proposed method. The 100 different cases are investigated at each S/N in changing a random seed. The parameters of the conventional neural network are set at $N_2 = 15$, $N_3 = 5$ and $T_{\text{NN}} = 10000$, where N_2 and N_3 denotes the number of neurons in the hidden and the output layers, respectively. As shown in Fig. 11, the proposed method significantly enhances the classification probability in the lower S/N, and has a substantial advantage over the conventional neural network based method.

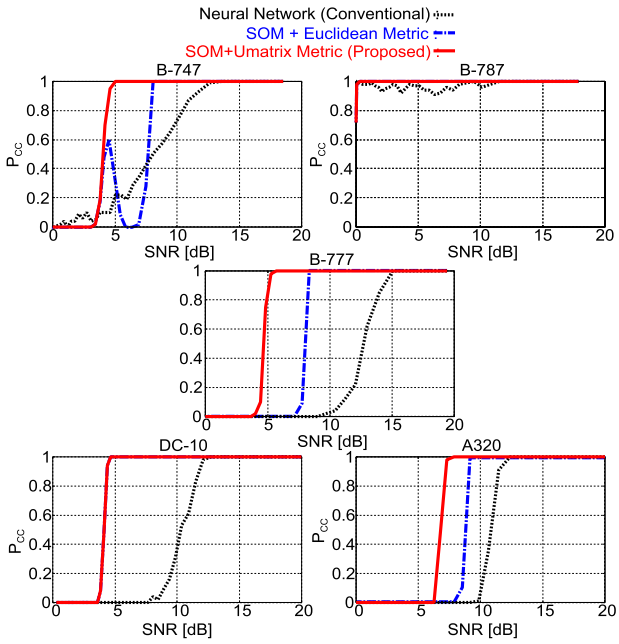

Fig. 11 Classification probability versus S/N for each airplane type.

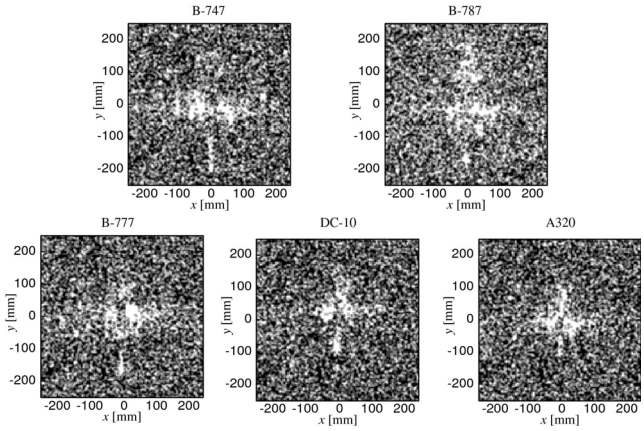

Fig. 12 Binarized images for each airplane at S/N = 8 dB.

Table 1 Required S/N for obtaining $P_{cc} \geq 0.9$ in each method.

	B747	B787	B777	DC-10	A320
Conventional	11 dB	5 dB	15 dB	12 dB	12 dB
Proposed	5 dB	0 dB	5 dB	5 dB	7 dB

As a reference, Fig. 11 includes the results obtained using the SOM based method with the traditional (Euclidean) metric, specifically, corresponding to $U(\boldsymbol{p}) = 1$ in Eq. (13). In the cases for the B-787 and DC-10, the same results are obtained using the traditional and U-matrix metrics. Except for these cases, it verifies that the U-matrix metric can enhance the P_{CC} in this classification problem, because not only does it measure the Euclidean distance between nodes, but can consider the actual potential barrier on the SOM generated by the U-matrix. It should be noted that the parameters used for the conventional method, such as the number of neurons in the hidden layer N_2 or the learning coefficient η, offer one of the best results in varying $N_2 = 10, 15, 20$ and 30 or $\eta = 1.0, 3.0$ and 5.0. Focusing on the results for the B-787, both methods retain a high P_{CC} over 0.9 for the lower S/N. This is because the SAR or binarized image of B-787, is particularly different from other images, due to the relatively high RCS from the airplane tail, and this difference makes the discrimination of B-787 easier in both methods, compared with other types of airplanes. For the particular case of S/N=8 dB, Figure 12 illustrates the binarized images for each airplane, contaminated by random noise, where the conventional method cannot offer a correct classification in any case, while the proposed method can do so even in quite noisy situations. Finally, Table 1 shows the comparison of the required S/N for holding the $P_{CC} = 0.9$ in each target case. This figure also verifies that the proposed method requires a S/N of less than 5 to 10 dB compared to the S/N required using the conventional method. This is because the proposed method not only evaluates the output disparity between the training and test outputs, but also assesses the topological distance on the SOM considering the potential barrier generated by the U-matrix.

5.2 Robustness to Observation Angle Errors

As further assessment of the ATR performance, the robustness to the angle difference of the observations is investigated. In this case, a nose angle of each airplane is ϕ as continuously varied from $-30°$ to $30°$ with $1°$ sampling, using the rotating table as shown in Fig. 6. Here, the same training process is carried out in both the conventional and proposed methods as in the previous evaluation, i.e., the SAR image at $\phi = 0°$ is employed as training data. The upper and lower side of Figs. 13, 14, 15, 16 and 17 present the classification results obtained by the conventional and the proposed methods, for the cases of the B-747, B-787, B-777, DC-10 and A320. The numerically generated noises are not considered in this case. These figures verify that the proposed method can significantly enhance the robustness related to observation angle errors, compared to those obtained by the conventional method, except for the case of B-787, which can easily be discriminated by both methods. This is because the topological metric considering the U-matrix field in the proposed method is considered to be effective in the case of the angular variations of observations. As an example of these results, Figure 18 shows the input images for each airplane in the case of $\phi = -15°$, where the proposed method correctly classifies all the images, while the conventional method does not offer any correct results, except for the B-787.

6. Conclusion

This paper proposed the SOM-based ATR method; it exploits the U-matrix metric to enhance the classification performance, especially in situations of low S/N or where the

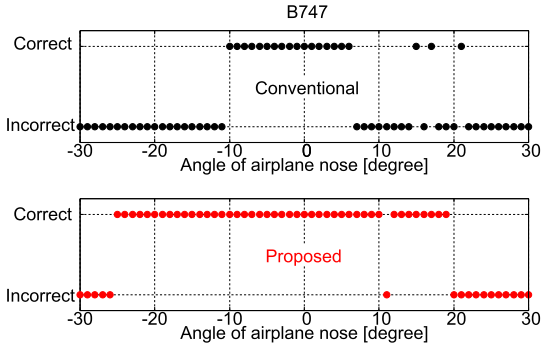

Fig. 13 Classification result for each angle of airplane nose in B747 obtained by the conventional (lower) and the proposed methods (upper).

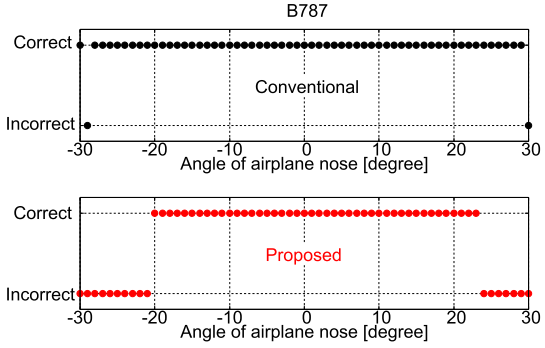

Fig. 14 Same view as in Fig. 13 in the case of B787.

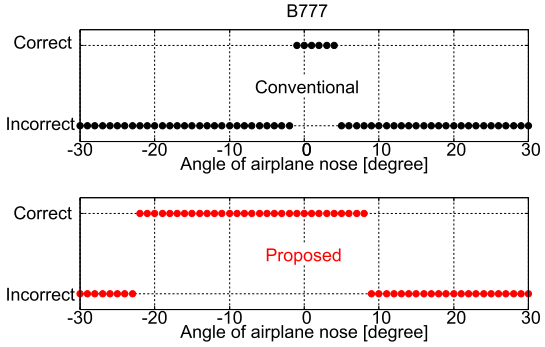

Fig. 15 Same view as in Fig. 13 in the case of B777.

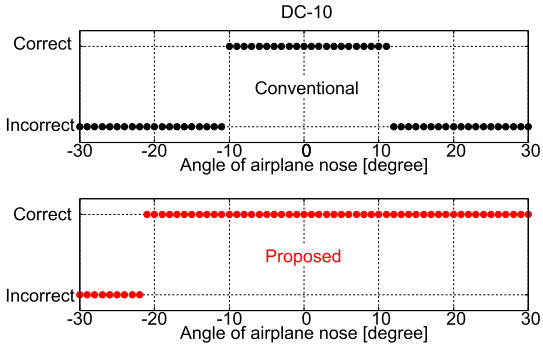

Fig. 16 Same view as in Fig. 13 in the case of DC-10.

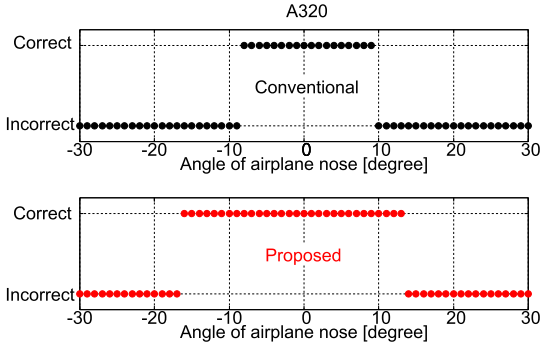

Fig. 17 Same view as in Fig. 13 in the case of A320.

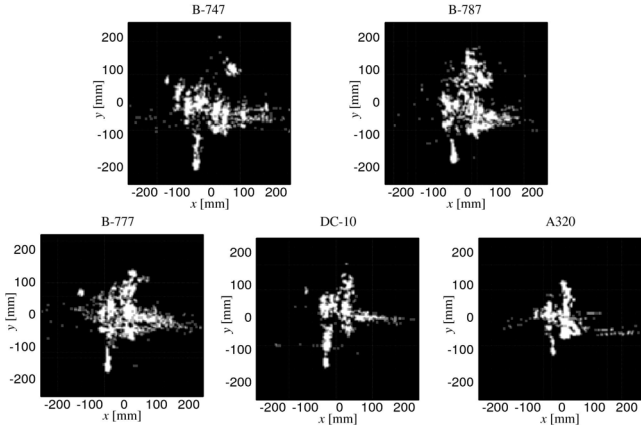

Fig. 18 Binarized images for each airplane at $\phi = -15°$.

orientations contain angle errors. The conventional neural network approach has the inevitable problem that in the lower S/N case, its classification performance is severely degraded because it can only compare the output value of the final layer in the classification process. By contrast, the proposed method measures the actual differences between the training and test binary images considering the topological distribution of U-matrix potential field. A performance evaluation, based on the experimental data investigating 5 types of typical civilian aircrafts, verified that the proposed method significantly enhances the classification probability compared to the conventional method, in the case of contaminated images by random noises or the situation that the observation angle for the target is different from that of the training images, and it is more flexible to the practical ATR applications. In addition, it is an important future work to assess our proposed method using the SAR images produced by the actual satellite-borne SAR systems.

References

[1] W.M. Brown, "Synthetic aperture radar," IEEE Trans. Aerosp. Electron. Syst., vol.AES-3, pp.217–229, March 1967.
[2] A.R. Brenner and L. Roessing, "Radar imaging of urban areas by means of very high-resolution SAR and interferometric SAR," IEEE Trans. Geosci. Remote Sens., vol.46, no.10, pp.2971–2982, Oct. 2008.
[3] A.A. Poposcu, I. Gavat, and M. Datcu, "Contextual descriptions for

scene classes in very high resolution SAR images," IEEE Geos. Remote Sens. Lett., vol.9, no.1, pp.80–84, Jan. 2012.
[4] D. Gross, "A neural network ATR for high range resolution radar signature recognition of moving ground targets," Proc. Signals, Systems, and Computers, 1999, Conference Record of the 33rd Asilomar Conference, vol.2, pp.1235–1239, Oct. 1999.
[5] Z. Gou and S. Li, "One-dimensional frequency-domain features for aircraft recognition from radar range profiles," IEEE Trans. Aerosp. Electron. Syst., vol.46, no.4, pp.1880–1892, Oct. 2010.
[6] X. Yu, Y. Li, and L.C. Jiao, "SAR automatic target recognition based on classifies fusion," Proc. 2011 International Workshop on Multi-Platform Multi-sensor Remote Sensing and Mapping, pp.1–5, Jan. 2011.
[7] C.M. Pilcher and A. Khotanzad, "Maritime ATR using classifier combination and high resolution range profiles," IEEE Trans. Aerosp. Electron. Syst., vol.47, no.4, pp.2558–2573, Oct. 2011.
[8] M. Martorella, E. Giusti, L. Demi, Z. Zhou, A. Cacciamano, F. Berizzi, and B. Bates, "Target recognition by means of polarimetric ISAR images," IEEE Trans. Aerosp. Electron. Syst., vol.47, no.1, pp.225–239, Jan. 2011.
[9] L.M. Novak, S.D. Halversen, G.J. Owirka, and M. Hiett, "Effects of polarization and resolution on SAR ATR," IEEE Trans. Aerosp. Electron. Syst., vol.33, no.1, pp.102–116, Jan. 1997.
[10] T. Kohonen, Self-Organizing Maps, vol.30, Springer, Berlin Heidelberg, Germany, 1995.
[11] J. Vesanto and E. Alhoniemi, "Clustering of the self-organizing map," IEEE Trans. Neural Netw., vol.11, no.3, pp.586–600, May 2000.
[12] M. Teranishi, S. Omatsu, and T. Kosaka, "Fatigue level estimation of bill by using supervised SOM based on feature selected acoustic energy pattern," IEEE Proc. Hybrid Intelligent Systems, 2008, pp.368–373, 2008.
[13] M. Hannula, J. Laitinen, and E. Alasaarela, "Classification accuracy of a frequency analysis method: Comparison between supervised SOM and KNN," IEEE Proc. Information Technology Applications in Biomedichine, 2003, pp.254–257, 2003.
[14] M. Hosokawa, Y. Ito, and T. Hoshi, "A remote sensing data classification method using self-organizing map," Proc. IEEE IGARSS 1999, pp.1606–1608, Aug. 1999.
[15] M. Hosokawa, Y. Ito, and T. Hoshi, "Extraction of urban characteristic using polarimetric SAR data and self-organizing map," IEICE Trans. Commun. (Japanese Edition), vol.J84-B, no.6, pp.1043–1051, June 2001.
[16] A. Ultsch, G. Guimaraes, D. Korus, and H. Li, "Knowledge extraction from artificial neural networks and applications," Proc. IEEE, vol.4, pp.3030–3035, Oct. 1997.
[17] A. Ultsch and H.P. Siemon, "Kohonen's self organizing feature maps for exploratory data analysis," Proc. International Neural Network Conference, pp.305–308, 1990.
[18] H. Matsushita and Y. Nishio, "Batch-learning self-organization map with false-neighbour degree between neurons," IEEE Proc. IJCNN 2008, pp.2259–2266, June 2008.
[19] L.M.H. Ulander, H. Hellsten, and G. Stenstrom, "Synthetic-aperture radar processing using fast factorized back-projection," IEEE Trans. Aerosp. Electron. Syst., vol.39, no.3, pp.760–776, July 2003.
[20] N. Otsu, "A threshold selection method from gray-level histograms," IEEE Trans. Syst. Man. Cybern., vol.9, no.1, pp.62–66, Jan. 1979.
[21] B. Widrow, R.G. Winter, and R.A. Baxter, "Layered neural nets for pattern recognition," IEEE Trans. Acoust. Speech Signal Process., vol.36, no.7, pp.1109–1118, July 1988.

Appendix: U-Matrix Field Calculation

U-matrix fields around the node location $\boldsymbol{p}$ are calculated based on the approach as [17],

$$U\left(\boldsymbol{p}+\frac{\Delta\boldsymbol{x}}{2}\right)=\|\boldsymbol{y}(\boldsymbol{p}+\Delta\boldsymbol{x})-\boldsymbol{y}(\boldsymbol{p})\|, \quad (\mathrm{A}\cdot 1)$$

$$U\left(\boldsymbol{p}-\frac{\Delta\boldsymbol{x}}{2}\right)=\|\boldsymbol{y}(\boldsymbol{p}-\Delta\boldsymbol{x})-\boldsymbol{y}(\boldsymbol{p})\|, \quad (\mathrm{A}\cdot 2)$$

$$U\left(\boldsymbol{p}+\frac{\Delta\boldsymbol{y}}{2}\right)=\|\boldsymbol{y}(\boldsymbol{p}+\Delta\boldsymbol{y})-\boldsymbol{y}(\boldsymbol{p})\|, \quad (\mathrm{A}\cdot 3)$$

$$U\left(\boldsymbol{p}-\frac{\Delta\boldsymbol{y}}{2}\right)=\|\boldsymbol{y}(\boldsymbol{p}-\Delta\boldsymbol{y})-\boldsymbol{y}(\boldsymbol{p})\|, \quad (\mathrm{A}\cdot 4)$$

$$U\left(\boldsymbol{p}+\frac{\Delta\boldsymbol{x}}{2}+\frac{\Delta\boldsymbol{y}}{2}\right)=+\frac{1}{2}\|\boldsymbol{y}(\boldsymbol{p}+\Delta\boldsymbol{x}+\Delta\boldsymbol{y})-\boldsymbol{y}(\boldsymbol{p})\| +\frac{1}{2}\|\boldsymbol{y}(\boldsymbol{p}+\Delta\boldsymbol{x})-\boldsymbol{y}(\boldsymbol{p}+\Delta\boldsymbol{y})\|, \quad (\mathrm{A}\cdot 5)$$

$$U\left(\boldsymbol{p}+\frac{\Delta\boldsymbol{x}}{2}-\frac{\Delta\boldsymbol{y}}{2}\right)=+\frac{1}{2}\|\boldsymbol{y}(\boldsymbol{p}+\Delta\boldsymbol{x}-\Delta\boldsymbol{y})-\boldsymbol{y}(\boldsymbol{p})\| +\frac{1}{2}\|\boldsymbol{y}(\boldsymbol{p}+\Delta\boldsymbol{x})-\boldsymbol{y}(\boldsymbol{p}-\Delta\boldsymbol{y})\|, \quad (\mathrm{A}\cdot 6)$$

$$U\left(\boldsymbol{p}-\frac{\Delta\boldsymbol{x}}{2}+\frac{\Delta\boldsymbol{y}}{2}\right)=+\frac{1}{2}\|\boldsymbol{y}(\boldsymbol{p}-\Delta\boldsymbol{x}+\Delta\boldsymbol{y})-\boldsymbol{y}(\boldsymbol{p})\| +\frac{1}{2}\|\boldsymbol{y}(\boldsymbol{p}-\Delta\boldsymbol{x})-\boldsymbol{y}(\boldsymbol{p}+\Delta\boldsymbol{y})\|, \quad (\mathrm{A}\cdot 7)$$

$$U\left(\boldsymbol{p}-\frac{\Delta\boldsymbol{x}}{2}-\frac{\Delta\boldsymbol{y}}{2}\right)=+\frac{1}{2}\|\boldsymbol{y}(\boldsymbol{p}-\Delta\boldsymbol{x}-\Delta\boldsymbol{y})-\boldsymbol{y}(\boldsymbol{p})\| +\frac{1}{2}\|\boldsymbol{y}(\boldsymbol{p}-\Delta\boldsymbol{x})-\boldsymbol{y}(\boldsymbol{p}-\Delta\boldsymbol{y})\|,$$

$$U(\boldsymbol{p})=0, \quad (\mathrm{A}\cdot 8)$$

where $\Delta\boldsymbol{x}=(\Delta x,0)$, $\Delta\boldsymbol{y}=(0,\Delta y)$, and Δx and Δy denote the intervals of each node $\boldsymbol{p}$ along x and y axis, respectively. Naturally, each number of x and y samples of $U(\boldsymbol{p})$ has $2M_X+1$, and $2M_Y+1$, respectively. In addition, this paper assumes the periodical structure of the U-matrix similar to SOM structure, in order to appropriately calculate the potential field at each end of nodes.

Shouhei Kidera received his B.E. degree in Electrical and Electronic Engineering from Kyoto University in 2003 and M.I. and Ph.D. degrees in Informatics from Kyoto University in 2005 and 2007, respectively. He is an assistant professor in Graduate School of Informatics and Engineering, University of Electro-Communications, Japan. His current research interest is in advanced signal processing for the near field radar, UWB radar. He is a member of the Institute of Electrical and Electronics Engineering (IEEE) and the Institute of Electrical Engineering of Japan (IEEJ).

Tetsuo Kirimoto received the B.S. and M.S. and Ph.D. degrees in Communication Engineering from Osaka University in 1976, 1978 and 1995, respectively. During 1978–2003 he stayed in Mitsubishi Electric Corp. to study radar signal processing. From 1982 to 1983, he stayed as a visiting scientist at the Remote Sensing Laboratory of the University of Kansas. From 2003 to 2007, he joined the University of Kitakyushu as a Professor. Since 2007, he has been with the University of Electro-Communications, where he is a Professor at the Graduate School of Informatics and Engineering. His current study interests include digital signal processing and its application to various sensor systems. Prof. Kirimoto is a senior member of IEEE and a member of SICE (The Society of Instrument and Control Engineers) of Japan.